COMMUN. MATH. SCI.
Vol. 18, No. 3, pp. 663–685

CONSTRAINT ENERGY MINIMIZING GENERALIZED MULTISCALE FINITE ELEMENT METHOD FOR DUAL CONTINUUM MODEL*

SIU WUN CHEUNG†, ERIC T. CHUNG‡, YALCHIN EFENDIEV§, WING TAT LEUNG¶, AND MARIA VASILYEVA‖

Abstract. The dual continuum model serves as a powerful tool in the modeling of subsurface applications. It allows a systematic coupling of various components of the solutions. The system is of multiscale nature as it involves high heterogeneous and high contrast coefficients. To numerically compute the solutions, some types of reduced order methods are necessary. We will develop and analyze a novel multiscale method based on the recent advances in multiscale finite element methods. Our method will compute multiple local multiscale basis functions per coarse region. The idea is based on some local spectral problems, which are important to identify high contrast channels, and an energy minimization principle. Using these concepts, we show that the basis functions are localized, even in the presence of high contrast long channels and fractures. In addition, we show that the convergence of the method depends only on the coarse mesh size. Finally, we present several numerical tests to show the performance.

Keywords. fractured porous media; dual continuum model; multiscale method; model reduction.

AMS subject classifications. 65M60; 65M12.

1. Introduction

Common in a wide variety of applications related to subsurface formations, one needs to perform numerical simulations in domains containing discrete fractures, faults and thin structures. The material properties within fractures can have a large difference from the material properties in the background media, which can also contain highly heterogeneous and high contrast regions. These large contrasts in material properties and the complex geometries of the fractures lead to difficulties in traditional numerical simulations due to the fact that solutions contain various scales and resolving these scales requires huge computational costs. Our goal in this paper is to construct and analyze reduced models for such problems. In classical upscaling approach, the computational domain is decomposed into coarse blocks, not necessarily resolving scales, and effective material property is computed for each coarse block [16, 47]. To compute effective material properties, some local problems are solved. However, it is known that one effective coefficient per coarse region is not enough to capture various properties of the solutions, especially for regions with fractures and high contrast heterogeneities. To overcome this drawback, the multi-continuum approaches are used [3, 5, 30, 43, 46, 49], where several effective medium properties are constructed. For example, in flow problems, separate equations for the flow in the background (called matrix) and the flow

*Received: July 28, 2018; Accepted (in revised form): November 18, 2019. Communicated by Shi Jin.

†Department of Mathematics, Texas A&M University, College Station, TX 77843, USA (tonycsw2905@math.tamu.edu).

‡Department of Mathematics, The Chinese University of Hong Kong, Shatin, New Territories, Hong Kong SAR, China (tschung@math.cuhk.edu.hk).

§Department of Mathematics & Institute for Scientific Computation (ISC), Texas A&M University, College Station, Texas, USA (efendiev@math.tamu.edu).

¶Institute of Computational Engineering and Sciences, University of Texas at Austin, Austin, USA (sidnet123@gmail.com).

‖Institute for Scientific Computation, Texas A&M University, College Station, TX 77843 and Department of Computational Technologies, North-Eastern Federal University, Yakutsk, Republic of Sakha (Yakutia), Russia, 677980 (vasilyevadotmdotv@gmail.com).

within fractures are derived, and these quantities are coupled by some interaction terms. The multi-continuum model thus provides a powerful tool for problems for subsurface applications with fractures. One important component of our approach is a local fine grid simulation, which is typical in many multiscale and numerical upscaling techniques. In general, a fine grid simulation involving flow and transport in heterogenous fracture media can be decomposed into two parts (we refer to [27] for an overview). First of all, an unstructured fine mesh is needed to model the geometries of the fractures and background heterogeneities. Secondly, using the fine mesh, the underlying physical model is discretized. There are in literature a variety of numerical approaches. For instances, in [4, 26, 29, 33], the standard Galerkin formulation is considered, in [19, 24, 34, 36], the mixed finite element method is considered, and in [18, 23], the discontinuous Galerkin method is considered. Moreover, in [6, 22, 28, 38, 40, 44], the finite volume scheme is investigated. A hybrid scheme combining the finite element method for the pressure equation and the finite volume method for the transport equation has also been considered [21, 37, 39].

Fluid flow in porous media with highly connected fracture network can be described by dual continuum models, where we have coupled system of equations for porous matrix and for fracture network with specific mass transfer between them [5, 15, 46]. Moreover, dual continuum models are used to describe a wide range of scientific and engineering applications, for example, complex processes in shale reservoirs, where such models are used to describe a complex interaction of the organic and inorganic matter [1, 2]. In simulations of the vuggy carbonate reservoirs, dual continuum models describe flow in vugs/cavities and surrounding media [45, 48, 50]. In real world applications, properties of the dual continuum models are highly heterogeneous and leads to the construction of the fine grids to also resolve small scale heterogeneity in level of mesh construction. Direct simulation on the fine grid is computationally expensive and some model reduction techniques should be used.

The reduced model we developed in this paper is motivated by the generalized multiscale finite element method (GMsFEM) [7, 9, 17], which can be seen as a generalization of the multiscale finite element method (MsFEM). We will construct multiscale basis functions that can couple various continua as well as effects of high contrast channels. The main idea of GMsFEM is to identify local dominant modes by the use of local spectral problems defined in some suitable snapshot spaces. These ideas are important in identifying influences of high contrast channels and regions, which are required to be represented individually by separate basis functions. In this regard, the GMsFEM shares some similarities with the multi-continuum approaches (see [10]). The idea of constructing local basis functions using spectral problem has also been used by various domain decomposition methods [20, 31, 32]. We remark that the convergence of the GMsFEM is related to the decay of the eigenvalues of the local spectral problems [14].

It is in general not an easy task to derive a multiscale method with a convergence depending only on the coarse mesh size and independent of scales and contrast. To obtain multiscale methods with mesh-dependent convergence, several approaches are considered in literature [8, 12, 25, 35, 41, 42]. The theory of GMsFEM motivates the use of local spectral problems to capture the effects of high contrast channels. This idea is also used in obtaining mesh-dependent convergence [8, 12, 25].

In this paper, we will develop and analyze a novel multiscale method for a dual continuum model with a convergence depending only on the coarse mesh size and independent of scales and contrast. Our ideas are motivated by the constraint energy minimizing generalized multiscale finite element method (CEM-GMsFEM) [8, 12]. There are

two ingredients of our methodology. First of all, we will construct a set of local auxiliary multiscale basis functions, as in GMsFEM. These functions are dominant eigenfunctions of local spectral problems, and the number of these functions is the same as the number of high contrast channels. We emphasize that this is the minimal number of degrees of freedoms required to represent channelized effects. We also remark that these eigenfunctions are crucial in the construction of localized basis functions. The second key component is multiscale basis functions. These functions are obtained by minimizing an energy functional subject to certain constraints. These constraints are formulated using the auxiliary functions with the purpose of obtaining localized multiscale basis functions. In particular, for each of the auxiliary function, the constraints require that the minimizer of the energy functional is orthogonal, in a weighted L^2 sense, to all other auxiliary functions except the selected one. For the selected auxiliary functions, the constraints require the minimizer of the energy functional to satisfy a normalized condition. Combining the effects of auxiliary functions and energy minimization, we show that the minimizer of the energy functional has exponential decay property, and is very small outside an oversampling region obtained by the support of the selected auxiliary function. Moreover, the resulting multiscale method obtained by a Galerkin formulation has a mesh-dependent convergence rate. We remark that one can also perform adaptivity as in [11, 13, 14].

The paper is organized as follows. In Section 2, we will introduce the dual continuum model. Our multiscale method will be presented in Section 3 and analyzed in Section 4. In Section 5, we will present some numerical tests. The paper ends with a conclusion in Section 6.

2. Dual continuum model

We consider the following dual continuum model [5, 15, 46]

$$\begin{aligned} c_1\frac{\partial p_1}{\partial t} - \operatorname{div}(\kappa_1\nabla p_1) + \sigma(p_1 - p_2) &= f_1, \\ c_2\frac{\partial p_2}{\partial t} - \operatorname{div}(\kappa_2\nabla p_2) - \sigma(p_1 - p_2) &= f_2, \end{aligned} \tag{2.1}$$

in a computational domain $\Omega \subset \mathbb{R}^2$. Here, for $i = 1,2$, c_i is the compressibility, p_i is the pressure, κ_i is the permeability, and f_i is the source function for the i-th continuum. In addition, the continua are coupled through the mass exchange, and σ is a parameter which accounts for the strength of mass transfer between the continua. One particular application of the dual continuum model (2.1) is to represent the global interactive effects of the unresolved fractures and the matrix.

Let Ω be a domain with high conductive channels (heterogeneous media)

$$\Omega = D_m^i \cup D_f^i, \quad D_f^i = \cup_{l=1}^{n_f} D_{f,l}^i \tag{2.2}$$

where indices m and f represent the two subdomains with low and high permeability, n_f is the number of high conductive channels, i is the continuum. We prescribe the initial condition $p_i(0,\cdot) = p_i^0$ in Ω and the boundary condition $p_i(t,\cdot) = 0$ on $\partial\Omega$ for $t > 0$. Furthermore, we have

$$\kappa_i(x) = \begin{cases} \kappa_i^m, & x \in D_m^i, \\ \kappa_{l,i}^f, & x \in D_{f,l}^i, \end{cases}, \quad c_i(x) = \begin{cases} c_i^m, & x \in D_m^i, \\ c_{l,i}^f, & x \in D_{f,l}^i, \end{cases}, \quad i = 1,2, \quad l = 1,\ldots,n_f,$$

where $\kappa_{l,i}^f$ and $c_{l,i}^f$ are the permeability and compressibility on the l-th channel for the continuum i in subdomain $D_{f,l}^i$; κ_i^m and c_i^m are the permeability and compressibility in

subdomain D_m^i. Here, we assume the permeability fields are uniformly bounded, i.e.

$$0<\underline{\kappa}\leq\kappa_i(x)\leq\overline{\kappa}\quad\text{for } x\in\Omega,\quad\text{for } i=1,2. \tag{2.3}$$

Let $V=[H_0^1(\Omega)]^2$. Also, for a subdomain $D\subset\Omega$, we denote the restriction of V on D by $V(D)$, and the subspace of $V(D)$ with zero trace on ∂D by $V_0(D)$. The weak formulation of 2.1 then reads: find $p=(p_1,p_2)$ such that $p(t,\cdot)\in V_0$ and

$$c\left(\frac{\partial p}{\partial t},v\right)+a_Q(p,v)=(f,v), \tag{2.4}$$

for all $v=(v_1,v_2)$ with $v(t,\cdot)\in V_0$. Here, $(\cdot,\cdot)$ denotes the standard $L^2(\Omega)$ inner product. Moreover, the bilinear forms are defined as:

$$\begin{aligned}
c_i(p_i,v_i)&=\int_{D_m^i}c_i^m p_i v_i\,dx+\sum_l\int_{D_{f,l}^i}c_{l,i}^f p_i v_i\,dx=\int_\Omega c_i(x)p_i v_i\,dx,\\
c(p,v)&=\sum_i c_i(p_i,v_i),\\
a_i(p_i,v_i)&=\int_{D_m^i}\kappa_i^m\nabla p_i\cdot\nabla v_i\,dx+\sum_l\int_{D_{f,l}^i}\kappa_{l,i}^f\nabla p_i\cdot\nabla v_i\,dx=\int_\Omega\kappa_i(x)\nabla p_i\cdot\nabla v_i\,dx,\\
a(p,v)&=\sum_i a_i(p_i,v_i),\\
q(p,v)&=\sum_i\sum_l\int_\Omega\sigma(p_i-p_l)v_i\,dx,\\
a_Q(p,v)&=a(p,v)+q(p,v),\quad (f,v)=\sum_i(f_i,v_i),
\end{aligned} \tag{2.5}$$

3. Method description

In this section, we will describe the details of our proposed method. To start with, we introduce the notions of coarse and fine meshes. We start with a usual partition $\mathcal{T}^H$ of Ω into finite elements, which does not necessarily resolve any multiscale features. The partition $\mathcal{T}^H$ is called a coarse grid and a generic element K in the partition $\mathcal{T}^H$ is called a coarse element. Moreover, $H>0$ is called the coarse mesh size. We let N_c be the number of coarse grid nodes and N be the number of coarse elements. We also denote the collection of all coarse grid edges by $\mathcal{E}^H$. We perform a refinement of $\mathcal{T}^H$ to obtain a fine grid $\mathcal{T}^h$, where $h>0$ is called the fine mesh size. It is assumed that the fine grid is sufficiently fine to resolve the solution. An illustration of the fine grid and the coarse grid and a coarse element are shown in Figure 3.1. We remark that the fine grid is only used in solving local problems numerically. In our analysis, the fine grid does not play a role as we assume that all local problems are solved continuously.

We define local bilinear forms on a coarse element K_j by:

$$\begin{aligned}
a_i^{(j)}(p_i,v_i)&=\int_{K_j}\kappa_i(x)\nabla p_i\cdot\nabla v_i\,dx,\\
a^{(j)}(p,v)&=\sum_i a_i^{(j)}(p_i,v_i),\\
q^{(j)}(p,v)&=\sum_i\sum_l\int_{K_j}\sigma(p_i-p_l)v_i\,dx,
\end{aligned}$$

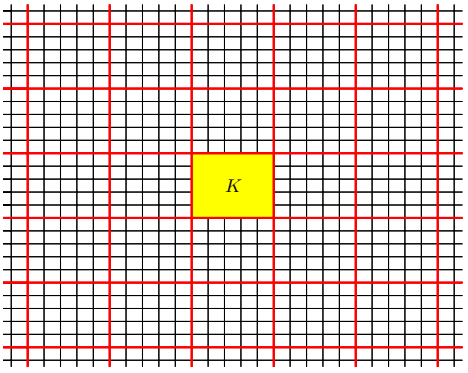

FIG. 3.1. *An illustration of the fine grid and the coarse grid and a coarse element.*

$$\begin{aligned} a_Q^{(j)}(p,v) &= a^{(j)}(p,v) + q^{(j)}(p,v), \\ s_i^{(j)}(p_i,v_i) &= \int_{K_j} \widetilde{\kappa}_i(x) p_i v_i \, dx, \\ s^{(j)}(p,v) &= \sum_i s_i^{(j)}(p_i,v_i), \end{aligned} \tag{3.1}$$

where $\widetilde{\kappa}_i = \kappa_i \sum_{k=1}^{N_c} |\nabla \chi_k|^2$ and $\{\chi_k\}$ is a set of bilinear partition of unity functions for the coarse grid partition of the domain Ω. We also define the bilinear form s by:

$$s(p,v) = \sum_j s^{(j)}(p,v). \tag{3.2}$$

Next, we will use the concept of GMsFEM to construct our auxiliary multiscale basis functions. The auxiliary basis functions are coupled, and defined by a spectral problem, which is to find a real number $\lambda_k^{(j)}$ and a function $\phi_k^{(j)} \in V(K_j)$ such that

$$a_Q^{(j)}(\phi_k^{(j)}, v) = \lambda_k^{(j)} s^{(j)}(\phi_k^{(j)}, v) \text{ for all } v \in V(K_j). \tag{3.3}$$

We let $\lambda_k^{(j)}$ be the eigenvalues of (3.3) arranged in ascending order in k, normalize the eigenfunctions in the norm induced by the inner product s, and use the first L_j eigenfunctions to construct our local auxiliary multiscale space

$$V_{aux}^{(j)} = \text{span}\{\phi_k^{(j)} : 1 \le k \le L_j\}. \tag{3.4}$$

The global auxiliary multiscale space V_{aux} is then defined as the sum of these local auxiliary multiscale spaces

$$V_{aux} = \oplus_{j=1}^{N} V_{aux}^{(j)}. \tag{3.5}$$

Before we move on to discuss the construction of multiscale basis functions, we introduce some tools which will be used to describe our method and analyze the convergence. We first introduce the notion of ϕ-orthogonality. In a coarse block K_j, given an auxiliary basis function $\phi_k^{(j)} \in V_{aux}$, we say that $\psi \in V$ is $\phi_k^{(j)}$-orthogonal if

$$s\left(\psi, \phi_{k'}^{(j')}\right) = \delta_{j,j'} \delta_{k,k'} \text{ for } 1 \le k' \le L_{j'} \text{ and } 1 \le j' \le N. \tag{3.6}$$

We also introduce a projection operator $\pi : [L^2(\Omega)]^2 \to V_{aux}$ by $\pi = \sum_{j=1}^{N} \pi_j$, where $\pi_j : [L^2(K_j)]^2 \to V_{aux}$ is given by

$$\pi_j(v) = \sum_{k=1}^{L_j} \frac{s^{(j)}(v, \phi_k^{(j)})}{s^{(j)}(\phi_k^{(j)}, \phi_k^{(j)})} \phi_k^{(j)} \text{ for all } v \in [L^2(K_j)]^2. \tag{3.7}$$

Next, we construct our global multiscale basis functions. The global multiscale basis function $\psi_j^{(i)} \in V$ is defined as the solution of the following constrained energy minimization problem

$$\psi_k^{(j)} = \operatorname{argmin} \left\{ a_Q(\psi, \psi) : \psi \in V \text{ is } \phi_k^{(j)}\text{-orthogonal} \right\}. \tag{3.8}$$

The minimization problem (3.8) is equivalent to the following variational problem: find $\psi_k^{(j)} \in V$ and $\mu_k^{(j)} \in V_{aux}$ such that

$$\begin{aligned} a_Q(\psi_k^{(j)}, w) + s(w, \mu_k^{(j)}) &= 0 \text{ for all } w \in V, \\ s(\psi_k^{(j)} - \phi_k^{(j)}, \nu) &= 0 \text{ for all } \nu \in V_{aux}. \end{aligned} \tag{3.9}$$

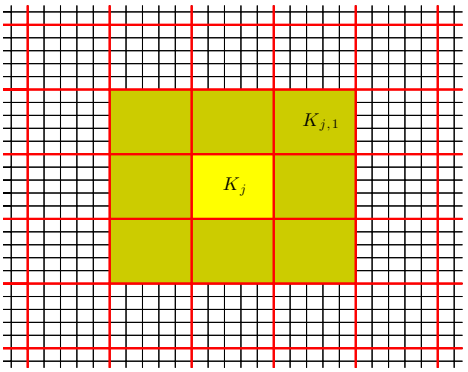

FIG. 3.2. *An illustration of an oversampled domain formed by enlarging K_j with 1 coarse grid layer.*

Motivated by the construction of global multiscale basis functions, we define our localized multiscale basis functions. For each element K_j, an oversampled domain formed by enlarging the coarse grid block K_j by m coarse grid layers. An illustration of an oversampled domain is shown in Figure 3.2. The localized multiscale basis function $\psi_{k,ms}^{(j)} \in V_0(K_{j,m})$ is defined as the solution of the following constrained energy minimization problem

$$\psi_{k,ms}^{(j)} = \operatorname{argmin} \left\{ a_Q(\psi, \psi) : \psi \in V_0(K_{j,m}) \text{ is } \phi_k^{(j)}\text{-orthogonal} \right\}. \tag{3.10}$$

The minimization problem (3.10) is equivalent to the following variational problem: find $\psi_{k,ms}^{(j)} \in V_0(K_{j,m})$ and $\mu_{k,ms}^{(j)} \in V_{aux}$ such that

$$\begin{aligned} a_Q(\psi_{k,ms}^{(j)}, w) + s(w, \mu_{k,ms}^{(j)}) &= 0 \text{ for all } w \in V_0(K_{j,m}), \\ s(\psi_{k,ms}^{(j)} - \phi_k^{(j)}, \nu) &= 0 \text{ for all } \nu \in V_{aux}. \end{aligned} \tag{3.11}$$

We use the localized multiscale basis functions to construct the multiscale finite element space, which is defined as

$$V_{ms} = \text{span}\{\psi_{k,ms}^{(j)} : 1 \le k \le L_j, 1 \le j \le N\}. \tag{3.12}$$

The multiscale solution is then given by: find $p_{ms} = (p_{ms,1}, p_{ms,2})$ with $p_{ms}(t,\cdot) \in V_{ms}$ such that for all $v = (v_1, v_2)$ with $v(t,\cdot) \in V_{ms}$,

$$c\left(\frac{\partial p_{ms}}{\partial t}, v\right) + a_Q(p_{ms}, v) = (f, v). \tag{3.13}$$

4. Convergence analysis

In this section, we will analyze the proposed method. First, we define the following norms and semi-norms on V:

$$\begin{aligned} \|p\|_c^2 &= c(p,p), \\ \|p\|_a^2 &= a(p,p), \\ |p|_q^2 &= q(p,p), \\ \|p\|_{a_Q}^2 &= a_Q(p,p), \\ \|p\|_s^2 &= s(p,p). \end{aligned} \tag{4.1}$$

For a subdomain $D = \bigcup_{j \in J} K_j$ composed by a union of coarse grid blocks, we also define the following local norms and semi-norms on V:

$$\begin{aligned} \|p\|_{a(D)}^2 &= \sum_{j \in J} a^{(j)}(p,p), \\ |p|_{q(D)}^2 &= \sum_{j \in J} q^{(j)}(p,p), \\ \|p\|_{a_Q(D)}^2 &= \sum_{j \in J} a_Q^{(j)}(p,p), \\ \|p\|_{s(D)}^2 &= \sum_{j \in J} s^{(j)}(p,p). \end{aligned} \tag{4.2}$$

The flow of our analysis goes as follows. First, we prove the convergence using the global multiscale basis functions. With the global multiscale basis functions constructed, the global multiscale finite element space is defined by

$$V_{glo} = \text{span}\{\psi_k^{(j)} : 1 \le k \le L_j, 1 \le j \le N\}, \tag{4.3}$$

and an approximated solution $p_{glo} = (p_{glo,1}, p_{glo,2})$, where $p_{glo}(t,\cdot) \in V_{glo}$, is given by

$$c\left(\frac{\partial p_{glo}}{\partial t}, v\right) + a_Q(p_{glo}, v) = (f, v), \tag{4.4}$$

for all $v = (v_1, v_2)$ with $v(t,\cdot) \in V_{glo}$. Next, we give an estimate of the difference between the global multiscale functions $\psi_k^{(j)}$ and the local multiscale basis functions $\psi_{k,ms}^{(j)}$, in order to show that using the multiscale solution p_{ms} provides similar convergence results as the global solution p_{glo}. For this purpose, we denote the kernel of the projection operator π by $\widetilde{V}$. Then, for any $\psi_k^{(j)} \in V_{glo}$, we have

$$a_Q(\psi_k^{(j)}, w) = 0 \text{ for all } w \in \widetilde{V}, \tag{4.5}$$

which implies $\widetilde{V} \subseteq V_{glo}^{\perp}$, where $V_{glo}^{\perp}$ is the orthogonal complement of V_{glo} with respect to the inner product a_Q. Moreover, since $\dim(V_{glo}) = \dim(V_{aux})$, we have $\widetilde{V} = V_{glo}^{\perp}$ and $V = V_{glo} \oplus \widetilde{V}$.

In addition, we introduce some operators which will be used in our analysis, namely $R_{glo}: V \to V_{glo}$ given by: for any $u \in V$, the image $R_{glo}u \in V_{glo}$ is defined by

$$a_Q(R_{glo}u, v) = a_Q(u, v) \text{ for all } v \in V_{glo}, \tag{4.6}$$

and similarly, $R_{ms}: V \to V_{ms}$ given by: for any $u \in V$, the image $R_{ms}u \in V_{ms}$ is defined by

$$a_Q(R_{ms}u, v) = a_Q(u, v) \text{ for all } v \in V_{ms}. \tag{4.7}$$

We also define $\mathcal{C}: V \to V$ given by: for any $u \in V$, the image $\mathcal{C}u \in V$ is defined by

$$(\mathcal{C}u, v) = c(u, v) \text{ for all } v \in V. \tag{4.8}$$

Moreover, the operator $\mathcal{A}: D(\mathcal{A}) \to [L^2(\Omega)]^2$ is defined on a subspace $D(\mathcal{A}) \subset V$ by: for any $u \in D(\mathcal{A})$, the image $\mathcal{A}u \in [L^2(\Omega)]^2$ is defined by

$$(\mathcal{A}u, v) = a_Q(u, v) \text{ for all } v \in V. \tag{4.9}$$

We will first show the projection operator R_{glo} onto global multiscale finite element space has a good approximation property with respect to the a_Q-norm and L^2-norm.

LEMMA 4.1. *Let $u \in D(\mathcal{A})$. Then we have $u - R_{glo}u \in \widetilde{V}$ and*

$$\|u - R_{glo}u\|_{a_Q} \leq CH\underline{\kappa}^{-\frac{1}{2}}\Lambda^{-\frac{1}{2}}\|\mathcal{A}u\|_{[L^2(\Omega)]^2}, \tag{4.10}$$

and

$$\|u - R_{glo}u\|_{[L^2(\Omega)]^2} \leq CH^2\underline{\kappa}^{-1}\Lambda^{-1}\|\mathcal{A}u\|_{[L^2(\Omega)]^2}, \tag{4.11}$$

where

$$\Lambda = \min_{1 \leq j \leq N} \lambda_{L_j+1}^{(j)}. \tag{4.12}$$

Proof. From (4.6), we see that $u - R_{glo}u \in V_{glo}^{\perp} = \widetilde{V}$. Taking $v = R_{glo}u \in V_{glo}$ in (4.6), we have

$$a_Q(u - R_{glo}u, R_{glo}u) = 0. \tag{4.13}$$

Therefore, we have

$$\begin{aligned} \|u - R_{glo}u\|_{a_Q}^2 &= a_Q(u - R_{glo}u, u - R_{glo}u) \\ &= a_Q(u - R_{glo}u, u) \\ &= a_Q(u, u - R_{glo}u) \\ &= (\mathcal{A}u, u - R_{glo}u) \\ &\leq \|\widetilde{\kappa}^{-\frac{1}{2}}\mathcal{A}u\|_{[L^2(\Omega)]^2}\|u - R_{glo}u\|_s, \end{aligned} \tag{4.14}$$

where $\widetilde{\kappa}(x)=\min\{\widetilde{\kappa}_i(x),\widetilde{\kappa}_{l,i}(x)\}$. Since $u-R_{glo}u\in\widetilde{V}$, we have $\pi_j(u-R_{glo}u)=0$ for all $j=1,2,\ldots,N$ and

$$\begin{aligned}\|u-R_{glo}u\|_s^2&=\sum_{j=1}^N\|u-R_{glo}u\|_{s(K_j)}^2\\&=\sum_{j=1}^N\|(I-\pi_j)(u-R_{glo}u)\|_{s(K_j)}^2.\end{aligned}\tag{4.15}$$

By the orthogonality of the eigenfunctions $\phi_k^{(j)}$, we have

$$\sum_{j=1}^N\|(I-\pi_j)(u-R_{glo}u)\|_{s(K_j)}^2\le\frac{1}{\Lambda}\sum_{j=1}^N\|u-R_{glo}u\|_{a_Q(K_j)}^2\le\frac{1}{\Lambda}\|u-R_{glo}u\|_{a_Q}^2.\tag{4.16}$$

Finally, using the fact that $|\nabla\chi_k|=O(H^{-1})$, we obtain the first estimate (4.10).

For the second estimate (4.11), we use a duality argument. Define $w\in V$ by

$$a_Q(w,v)=(u-R_{glo}u,v)\text{ for all }v\in V.\tag{4.17}$$

Then we have

$$\|u-R_{glo}u\|_{[L^2(\Omega)]^2}^2=(u-R_{glo}u,u-R_{glo}u)=a_Q(w,u-R_{glo}u).\tag{4.18}$$

Taking $v=R_{glo}w\in V_{glo}$ in (4.6), we have

$$a_Q(u-R_{glo}u,R_{glo}w)=0.\tag{4.19}$$

Note that $w\in D(\mathcal{A})$ and $\mathcal{A}w=u-R_{glo}u$. Hence

$$\begin{aligned}\|u-R_{glo}u\|_{[L^2(\Omega)]^2}^2&=a_Q(w-R_{glo}w,u-R_{glo}u)\\&\le\|w-R_{glo}w\|_{a_Q}\|u-R_{glo}u\|_{a_Q}\\&\le\left(CH\underline{\kappa}^{-\frac{1}{2}}\Lambda^{-\frac{1}{2}}\|\mathcal{A}w\|_{[L^2(\Omega)]^2}\right)\left(CH\underline{\kappa}^{-\frac{1}{2}}\Lambda^{-\frac{1}{2}}\|\mathcal{A}u\|_{[L^2(\Omega)]^2}\right)\\&\le CH^2\underline{\kappa}^{-1}\Lambda^{-1}\|u-R_{glo}u\|_{[L^2(\Omega)]^2}\|\mathcal{A}u\|_{[L^2(\Omega)]^2}.\end{aligned}\tag{4.20}$$

∎

We remark that the quantity Λ is contrast independent as we include all eigenfunctions corresponding to small contrast-dependent eigenvalues in our basis construction.

We are now going to prove the global basis functions are localizable. For each coarse block K, we define B to be a bubble function with $B(x)>0$ for all $x\in\text{int}(K)$ and $B(x)=0$ for all $x\in\partial K$. We will take $B=\prod_j\chi_j^{ms}$ where the product is taken over all vertices j on the boundary of K, and $\{\chi_j\}$ is a set of bilinear partition of unity functions for the coarse grid partition of the domain Ω. Using the bubble function, we define the constant

$$C_\pi=\sup_{K\in\mathcal{T}^H,\nu\in V_{aux}}\frac{s(\nu,\nu)}{s(B\nu,\nu)}.\tag{4.21}$$

We also define

$$\lambda_{max}=\max_{1\le j\le N}\max_{1\le k\le L_j}\lambda_k^{(j)}.\tag{4.22}$$

LEMMA 4.2. *For all $v_{aux} \in V_{aux}$, there exists a function $v \in V$ such that*

$$\pi(v) = v_{aux}, \quad \|v\|_{a_Q}^2 \leq D\|v_{aux}\|_s^2, \quad supp(v) \subset supp(v_{aux}). \tag{4.23}$$

We write $D = 2(1+2C_p^2\sigma_{\underline{\kappa}}^{-1})(C_{\mathcal{T}}+\lambda_{max}^2)$, where $C_{\mathcal{T}}$ is the square of the maximum number of vertices over all coarse elements, and C_p is a Poincaré constant.

Proof. Let $v_{aux} \in V_{aux}^{(j)}$ with $\|v_{aux}\|_{s(K_j)} = 1$. We consider the following minimization problem defined on a coarse block K_j.

$$v = \text{argmin}\left\{a_Q(\psi,\psi) : \psi \in V_0(K_j), \quad s^{(j)}(\psi,\nu) = s^{(j)}(v_{aux},\nu) \text{ for all } \nu \in V_{aux}^{(j)}\right\}. \tag{4.24}$$

We will show that the minimization problem (4.24) has a unique solution. First, we note that the minimization problem (4.24) is equivalent to the following variational problem: find $v \in V_0(K_j)$ and $\mu \in V_{aux}^{(j)}$ such that

$$\begin{aligned} a_Q^{(j)}(v,w) + s^{(j)}(w,\mu) &= 0 \text{ for all } w \in V_0(K_j), \\ s^{(j)}(v - v_{aux},\nu) &= 0 \text{ for all } \nu \in V_{aux}^{(j)}. \end{aligned} \tag{4.25}$$

The well-posedness of (4.25) is equivalent to the existence of $v \in V_0(K_j)$ such that

$$s^{(j)}(v,v_{aux}) \geq C\|v_{aux}\|_{s(K_j)}^2, \quad \|v\|_{a_Q(K_j)} \leq C\|v_{aux}\|_{s(K_j)}, \tag{4.26}$$

where C is a constant to be determined. Now, we take $v = Bv_{aux} \in V_0(K_j)$. Then we have

$$s^{(j)}(v,v_{aux}) = s^{(j)}(Bv_{aux},v_{aux}) \geq C_\pi^{-1} s\|v_{aux}\|_{s(K_j)}^2. \tag{4.27}$$

On the other hand, since $\nabla v_i = \nabla(Bv_{aux,i}) = v_{aux,i}\nabla B + B\nabla v_{aux,i}$, $|B| \leq 1$ and $|\nabla B|^2 \leq C_{\mathcal{T}}\sum_k |\nabla \chi_k^{ms}|^2$, we have

$$\|v\|_{a(K_j)}^2 \leq 2(C_{\mathcal{T}}\|v_{aux}\|_{s(K_j)}^2 + \|v_{aux}\|_{a_Q(K_j)}^2). \tag{4.28}$$

By the spectral problem (3.3), we have

$$\|v_{aux}\|_{a_Q(K_j)} \leq \max_{1\leq k\leq L_j} \lambda_k^{(j)} \|v_{aux}\|_{s(K_j)}. \tag{4.29}$$

Moreover, by Poincaré inequality, we have

$$|v|_q^2 \leq 2\sigma\|v\|_{L^2(K_j)}^2 \leq 2C_p^2\sigma_{\underline{\kappa}}^{-1}\|v\|_{a(K_j)}^2. \tag{4.30}$$

Combining these estimates, we have

$$\|v\|_{a_Q(K_j)}^2 \leq (1+2C_p^2\sigma_{\underline{\kappa}}^{-1})\|v\|_{a(K_j)}^2 \leq 2(1+2C_p^2\sigma_{\underline{\kappa}}^{-1})(C_{\mathcal{T}}+\lambda_{max}^2)\|v_{aux}\|_{s(K_j)}^2. \tag{4.31}$$

This shows that the minimization problem (4.24) has a unique solution $v \in V_0(K_j)$, which satisfies our desired properties. ∎

Here, we make a remark that we can assume $D \geq 1$ without loss of generality.

In order to estimate the difference between the global basis functions and localized basis functions, we need the notion of a cutoff function with respect to the oversampling

regions. For each coarse grid K_j and $M>m$, we define $\chi_j^{M,m}\in\text{span}\{\chi_k^{ms}\}$ such that $0\leq\chi_j^{M,m}\leq 1$ and $\chi_j^{M,m}=1$ on the inner region $K_{j,m}$ and $\chi_j^{M,m}=0$ outside the region $K_{j,M}$.

The following lemma shows that our multiscale basis functions have a decay property. In particular, the global basis functions are small outside an oversampled region specified in the lemma, which is important in localizing the multiscale basis functions.

LEMMA 4.3. *Given $\phi_k^{(j)}\in V_{aux}^{(j)}$ and an oversampling region $K_{j,m}$ with number of layers $m\geq 2$. Let $\psi_{k,ms}^{(j)}$ be a localized multiscale basis function defined on $K_{j,m}$ given by (3.10), and $\psi_k^{(j)}$ be the corresponding global basis function given by (3.8). Then we have*

$$\|\psi_k^{(j)}-\psi_{k,ms}^{(j)}\|_{a_Q}^2\leq E\|\phi_k^{(j)}\|_{s(K_j)}^2, \tag{4.32}$$

where $E=24D^2(1+\Lambda^{-1})\left(1+\dfrac{\Lambda^{\frac{1}{2}}}{2D^{\frac{1}{2}}}\right)^{1-m}$.

Proof. By Lemma 4.2, there exists $\widetilde{\phi}_k^{(j)}\in V$ such that

$$\pi(\widetilde{\phi}_k^{(j)})=\phi_k^{(j)},\quad \|\widetilde{\phi}_k^{(j)}\|_{a_Q}^2\leq D\|\phi_k^{(j)}\|_s^2,\quad \text{supp}(\widetilde{\phi}_k^{(j)})\subset K_j. \tag{4.33}$$

We take $\eta=\psi_k^{(j)}-\widetilde{\phi}_k^{(j)}\in V$ and $\zeta=\widetilde{\phi}_k^{(j)}-\psi_{k,ms}^{(j)}\in V_0(K_{j,m})$. Then $\pi(\eta)=\pi(\zeta)=0$ and hence $\eta,\zeta\in\widetilde{V}$. Again, by Lemma 4.2, there exists $\beta\in V$ such that

$$\pi(\beta)=\pi(\chi_j^{m,m-1}\eta),\quad \|\beta\|_{a_Q}^2\leq D\|\pi(\chi_j^{m,m-1}\eta)\|_s^2,\quad \text{supp}(\beta)\subset K_{j,m}\setminus K_{j,m-1}. \tag{4.34}$$

Take $\tau=\beta-\chi_j^{m,m-1}\eta\in V_0(K_{j,m})$. Again, $\pi(\tau)=0$ and hence $\tau\in\widetilde{V}$. Now, by the variational problems (3.9) and (3.11), we have

$$a_Q(\psi_k^{(j)}-\psi_{k,ms}^{(j)},w)+s(w,\mu_k^{(j)}-\mu_{k,ms}^{(j)})=0 \text{ for all } w\in V_0(K_{j,m}). \tag{4.35}$$

Taking $w=\tau-\zeta\in V_0(K_{j,m})$ and using the fact that $\tau-\zeta\in\widetilde{V}$, we have

$$a_Q(\psi_k^{(j)}-\psi_{k,ms}^{(j)},\tau-\zeta)=0, \tag{4.36}$$

which implies

$$\begin{aligned}\|\psi_k^{(j)}-\psi_{k,ms}^{(j)}\|_{a_Q}^2&=a_Q(\psi_k^{(j)}-\psi_{k,ms}^{(j)},\psi_k^{(j)}-\psi_{k,ms}^{(j)})\\&=a_Q(\psi_k^{(j)}-\psi_{k,ms}^{(j)},\eta+\zeta)\\&=a_Q(\psi_k^{(j)}-\psi_{k,ms}^{(j)},\eta+\tau)\\&\leq\|\psi_k^{(j)}-\psi_{k,ms}^{(j)}\|_{a_Q}\|\eta+\tau\|_{a_Q}.\end{aligned} \tag{4.37}$$

Therefore, we have

$$\begin{aligned}\|\psi_k^{(j)}-\psi_{k,ms}^{(j)}\|_{a_Q}^2&\leq\|\eta+\tau\|_{a_Q}^2\\&=\|(1-\chi_j^{m,m-1})\eta+\beta\|_{a_Q}^2\\&\leq 2\left(\|(1-\chi_j^{m,m-1})\eta\|_{a_Q}^2+\|\beta\|_{a_Q}^2\right).\end{aligned} \tag{4.38}$$

For the first term on the right-hand side of (4.38), since $\nabla\left((1-\chi_j^{m,m-1})\eta_i\right)=(1-\chi_j^{m,m-1})\nabla\eta_i-\eta_i\nabla\chi_j^{m,m-1}$ and $|1-\chi_j^{m,m-1}|\leq 1$, we have

$$\|(1-\chi_j^{m,m-1})\eta_i\|_{a_i}^2\leq 2\left(\|\eta_i\|_{a_i(\Omega\setminus K_{j,m-1})}^2+\|\eta_i\|_{s_i(\Omega\setminus K_{j,m-1})}^2\right). \tag{4.39}$$

On the other hand, we have

$$|(1-\chi_j^{m,m-1})\eta|_q^2\leq|\eta|_{q(\Omega\setminus K_{j,m-1})}^2. \tag{4.40}$$

For the second term on the right-hand side of (4.38), we first see that for $K_{j'}\subset K_{j,m-1}$,

$$s\left(\chi_j^{m,m-1}\eta,\phi_k^{(j')}\right)=s^{(j')}\left(\chi_j^{m,m-1}\eta,\phi_k^{(j')}\right)=s^{(j')}\left(\eta,\phi_k^{(j')}\right)=0, \tag{4.41}$$

since $\chi_j^{m,m-1}=1$ on $K_{j,m-1}$ and $\eta\in\widetilde{V}$. On the other hand, for $K_{j'}\subset\Omega\setminus K_{j,m}$,

$$s\left(\chi_j^{m,m-1}\eta,\phi_k^{(j')}\right)=s^{(j')}\left(\chi_j^{m,m-1}\eta,\phi_k^{(j')}\right)=0, \tag{4.42}$$

since $\chi_j^{m,m-1}=0$ on $\Omega\setminus K_{j,m}$. Therefore, we have $\operatorname{supp}\left(\pi(\chi_j^{m,m-1}\eta)\right)\subset K_{j,m}\setminus K_{j,m-1}$. Using (4.34) and $|\chi_j^{m,m-1}|\leq 1$, we have

$$\begin{aligned}\|\beta\|_{a_Q}^2&\leq D\|\pi(\chi_j^{m,m-1}\eta)\|_{s(K_{j,m}\setminus K_{j,m-1})}^2\\&\leq D\|\chi_j^{m,m-1}\eta\|_{s(K_{j,m}\setminus K_{j,m-1})}^2\\&\leq D\|\eta\|_{s(K_{j,m}\setminus K_{j,m-1})}^2.\end{aligned} \tag{4.43}$$

Since $\eta\in\widetilde{V}$, by the spectral problem (3.3), we obtain

$$\|\eta\|_{s(K_{j,m}\setminus K_{j,m-1})}^2\leq\Lambda^{-1}\|\eta\|_{a_Q(\Omega\setminus K_{j,m-1})}^2. \tag{4.44}$$

Combining these estimates, we have

$$\begin{aligned}\|\psi_k^{(j)}-\psi_{k,ms}^{(j)}\|_{a_Q}^2&\leq(4+4\Lambda^{-1}+2D\Lambda^{-1})\|\eta\|_{a_Q(\Omega\setminus K_{j,m-1})}^2\\&\leq 6D(1+\Lambda^{-1})\|\eta\|_{a_Q(\Omega\setminus K_{j,m-1})}^2.\end{aligned} \tag{4.45}$$

Next, we will prove a recursive estimate for $\|\eta\|_{a_Q(\Omega\setminus K_{j,m-1})}^2$. We take $\xi=1-\chi_j^{m-1,m-2}$.

Then $\xi=1$ in $\Omega\setminus K_{j,m-1}$ and $0\leq\xi\leq 1$. Hence, using $\nabla(\xi^2\eta_i)=\xi^2\nabla\eta_i+2\xi\eta_i\nabla\xi$, we have

$$|\xi\eta|_a^2=a(\eta,\xi^2\eta)+\|\eta\|_{s(K_{j,m-1}\setminus K_{j,m-2})}^2, \tag{4.46}$$

which results in

$$\|\eta\|_{a_Q(\Omega\setminus K_{j,m-1})}^2\leq\|\xi\eta\|_{a_Q}^2\leq a_Q(\eta,\xi^2\eta)+\|\eta\|_{s(K_{j,m-1}\setminus K_{j,m-2})}^2. \tag{4.47}$$

We will estimate the first term on the right-hand side of (4.47). First, we note that, for any coarse element $K_{j'}\subset\Omega\setminus K_{j,m-1}$, since $\xi=1$ in $K_{j'}$ and $\eta\in\widetilde{V}$, we have

$$s\left(\xi^2\eta,\phi_{k'}^{(j')}\right)=s\left(\eta,\phi_{k'}^{(j')}\right)=0\text{ for all }k'=1,2,\ldots,L_{j'}. \tag{4.48}$$

On the other hand, for any coarse element $K_{j'} \subset K_{j,m-2}$, since $\xi = 0$ in $K_{j,m-2}$, we have

$$s\left(\xi^2\eta, \phi_{k'}^{(j')}\right) = 0 \text{ for all } k' = 1,2,\ldots,L_{j'}. \tag{4.49}$$

Therefore, $\text{supp}(\pi(\xi^2\eta)) \subset K_{j,m-1} \setminus K_{j,m-2}$. By Lemma 4.2, there exists $\gamma \in V$ such that

$$\pi(\gamma) = \pi(\xi^2\eta), \quad \|\gamma\|_{a_Q}^2 \leq D\|\pi(\xi^2\eta)\|_s^2, \quad \text{supp}(\gamma) \subset K_{j,m-1} \setminus K_{j,m-2}. \tag{4.50}$$

Take $\theta = \xi^2\eta - \gamma$. Again, $\pi(\theta) = 0$ and hence $\theta \in \widetilde{V}$. Therefore, we have

$$a_Q(\psi_k^{(j)}, \theta) = 0. \tag{4.51}$$

Additionally, $\text{supp}(\theta) \subset \Omega \setminus K_{j,m-2}$. Recall that, in (4.33), we have $\text{supp}(\widetilde{\phi}_k^{(j)}) \subset K_j$. Hence θ and $\widetilde{\phi}_k^{(j)}$ have disjoint supports, and

$$a_Q(\widetilde{\phi}_k^{(j)}, \theta) = 0. \tag{4.52}$$

Therefore, we obtain

$$a_Q(\eta, \theta) = a_Q(\psi_k^{(j)}, \theta) - a_Q(\widetilde{\phi}_k^{(j)}, \theta) = 0. \tag{4.53}$$

Note that $\xi^2\eta = \theta + \gamma$. Using (4.50), we have

$$\begin{aligned} a_Q(\eta, \xi^2\eta) &= a_Q(\eta, \gamma) \\ &\leq \|\eta\|_{a_Q(K_{j,m-1}\setminus K_{j,m-2})} \|\gamma\|_{a_Q(K_{j,m-1}\setminus K_{j,m-2})} \\ &\leq D^{\frac{1}{2}} \|\eta\|_{a_Q(K_{j,m-1}\setminus K_{j,m-2})} \|\pi(\xi^2\eta)\|_{s(K_{j,m-1}\setminus K_{j,m-2})}. \end{aligned} \tag{4.54}$$

For any coarse element $K_{j'} \subset K_{j,m-1} \setminus K_{j,m-2}$, since $\pi(\eta) = 0$, we have

$$\|\pi(\xi^2\eta)\|_{s(K_{j'})} \leq \|\xi^2\eta\|_{s(K_{j'})} \leq \|\eta\|_{s(K_{j'})} \leq \Lambda^{-\frac{1}{2}} \|\eta\|_{a_Q(K_{j'})}. \tag{4.55}$$

Summing up over all $K_{j'} \subset K_{j,m-1} \setminus K_{j,m-2}$, we obtain

$$\|\pi(\xi^2\eta)\|_{s(K_{j,m-1}\setminus K_{j,m-2})} \leq \Lambda^{-\frac{1}{2}} \|\eta\|_{a_Q(K_{j,m-1}\setminus K_{j,m-2})}. \tag{4.56}$$

Hence, the first term on the right-hand side of (4.47) can be estimated by

$$a(\eta, \xi^2\eta) \leq D^{\frac{1}{2}} \Lambda^{-\frac{1}{2}} \|\eta\|_{a_Q(K_{j,m-1}\setminus K_{j,m-2})}^2. \tag{4.57}$$

For the second term on the right-hand side of (4.47), a similar argument gives $\text{supp}(\xi\eta) \subset K_{j,m-1} \setminus K_{j,m-2}$, and

$$\|\eta\|_{s(K_{j,m-1}\setminus K_{j,m-2})} \leq \Lambda^{-\frac{1}{2}} \|\eta\|_{a_Q(K_{j,m-1}\setminus K_{j,m-2})}. \tag{4.58}$$

Putting (4.47), (4.57) and (4.58) together, we have

$$\|\eta\|_{a_Q(\Omega\setminus K_{j,m-1})}^2 \leq (1 + D^{\frac{1}{2}}) \Lambda^{-\frac{1}{2}} \|\eta\|_{a_Q(K_{j,m-1}\setminus K_{j,m-2})}^2 \leq 2D^{\frac{1}{2}} \Lambda^{-\frac{1}{2}} \|\eta\|_{a_Q(K_{j,m-1}\setminus K_{j,m-2})}^2. \tag{4.59}$$

Therefore,

$$\|\eta\|^2_{a_Q(\Omega\setminus K_{j,m-2})}=\|\eta\|^2_{a_Q(\Omega\setminus K_{j,m-1})}+\|\eta\|^2_{a_Q(K_{j,m-1}\setminus K_{j,m-2})}\geq\left(1+\frac{\Lambda^{\frac{1}{2}}}{2D^{\frac{1}{2}}}\right)\|\eta\|^2_{a_Q(\Omega\setminus K_{j,m-1})}. \tag{4.60}$$

Inductively, we have

$$\|\eta\|^2_{a_Q(\Omega\setminus K_{j,m-1})}\leq\left(1+\frac{\Lambda^{\frac{1}{2}}}{2D^{\frac{1}{2}}}\right)^{1-m}\|\eta\|^2_{a_Q(\Omega\setminus K_j)}\leq\left(1+\frac{\Lambda^{\frac{1}{2}}}{2D^{\frac{1}{2}}}\right)^{1-m}\|\eta\|^2_{a_Q}. \tag{4.61}$$

Finally, by the energy-minimizing property of $\psi_k^{(j)}$ and (4.33), we have

$$\|\eta\|_{a_Q}=\|\psi_k^{(j)}-\widetilde{\phi}_k^{(j)}\|_{a_Q}\leq 2\|\widetilde{\phi}_k^{(j)}\|_{a_Q}\leq 2D^{\frac{1}{2}}\|\phi_k^{(j)}\|_{s(K_j)}. \tag{4.62}$$

Combining (4.45), (4.61) and (4.62), we obtain our desired result. ∎

The above lemma motivates us to define localized multiscale basis functions in (3.10). The following lemma suggests that, similar to the projection operator R_{glo} onto the global multiscale finite element space, the projection operator R_{ms} onto our localized multiscale finite element space also has a good approximation property with respect to the a_Q-norm and L^2-norm.

LEMMA 4.4. *Let $u\in D(\mathcal{A})$. Let $m\geq 2$ be the number of coarse grid layers in the oversampling regions in (3.10). If $m=O\left(\log\left(\frac{\overline{\kappa}}{H}\right)\right)$, then we have*

$$\|u-R_{ms}u\|_{a_Q}\leq CH\underline{\kappa}^{-\frac{1}{2}}\Lambda^{-\frac{1}{2}}\|\mathcal{A}u\|_{[L^2(\Omega)]^2}, \tag{4.63}$$

and

$$\|u-R_{ms}u\|_{[L^2(\Omega)]^2}\leq CH^2\underline{\kappa}^{-1}\Lambda^{-1}\|\mathcal{A}u\|_{[L^2(\Omega)]^2}. \tag{4.64}$$

Proof. We write $R_{glo}u=\sum_{j=1}^N\sum_{k=1}^{L_j}\alpha_k^{(j)}\psi_k^{(j)}$, and define $w=\sum_{j=1}^N\sum_{k=1}^{L_j}\alpha_k^{(j)}\psi_{k,ms}^{(j)}\in V_{ms}$. By the Galerkin orthogonality in (4.7), we have

$$\|u-R_{ms}u\|_{a_Q}\leq\|u-w\|_{a_Q}\leq\|u-R_{glo}u\|_{a_Q}+\|R_{glo}u-w\|_{a_Q}. \tag{4.65}$$

Using Lemma 4.3, we see that

$$\begin{aligned}\|R_{glo}u-w\|^2_{a_Q}&=\left\|\sum_{j=1}^N\sum_{k=1}^{L_j}\alpha_k^{(j)}(\psi_k^{(j)}-\psi_{k,ms}^{(j)})\right\|^2_{a_Q}\\&\leq(2m+1)^d\sum_{j=1}^N\left\|\sum_{k=1}^{L_j}\alpha_k^{(j)}(\psi_k^{(j)}-\psi_{k,ms}^{(j)})\right\|^2_{a_Q}\\&\leq E(2m+1)^d\sum_{j=1}^N\left\|\sum_{k=1}^{L_j}\alpha_k^{(j)}\phi_k^{(j)}\right\|^2_{s}\end{aligned}$$

$$= E(2m+1)^d \|R_{glo}u\|_s^2, \tag{4.66}$$

where the last equality follows from the orthogonality of the eigenfunctions in (3.3). Combining (4.65), (4.66), together with (4.10) in Lemma 4.1, we have

$$\|u - R_{ms}u\|_{a_Q} \leq CH\underline{\kappa}^{-\frac{1}{2}}\Lambda^{-\frac{1}{2}}\|\mathcal{A}u\|_{[L^2(\Omega)]^2} + E^{\frac{1}{2}}(2m+1)^{\frac{d}{2}}\|R_{glo}u\|_s. \tag{4.67}$$

Next, we are going to estimate $\|R_{glo}u\|_s$. Using the fact that $|\nabla\chi_k| = O(H^{-1})$, we have

$$\|R_{glo}u\|_s^2 \leq CH^{-2}\overline{\kappa}\|R_{glo}u\|_{[L^2(\Omega)]^2}^2. \tag{4.68}$$

Then, by Poincaré inequality, we have

$$\|R_{glo}u\|_{[L^2(\Omega)]^2}^2 \leq C_p\underline{\kappa}^{-1}\|R_{glo}u\|_{a_Q}^2. \tag{4.69}$$

By taking $v = R_{glo}u$ in (4.6), we obtain

$$\|R_{glo}u\|_{a_Q}^2 = a_Q(u, R_{glo}u) = (\mathcal{A}u, R_{glo}u) \leq CH\underline{\kappa}^{-\frac{1}{2}}\|\mathcal{A}u\|_{[L^2(\Omega)]^2}\|R_{glo}u\|_s. \tag{4.70}$$

Combining these estimates, we have

$$\|R_{glo}u\|_s \leq CH^{-1}\overline{\kappa}\underline{\kappa}^{-\frac{1}{2}}\|\mathcal{A}u\|_{[L^2(\Omega)]^2}. \tag{4.71}$$

To obtain our desired result, we need

$$H^{-2}\overline{\kappa}(2m+1)^{\frac{d}{2}}E^{\frac{1}{2}} = O(1). \tag{4.72}$$

Taking logarithm, we have

$$\log(H^{-2}) + \log(\overline{\kappa}) + \frac{d}{2}\log(2m+1) + \frac{1-m}{2}\log\left(1 + \frac{\Lambda^{\frac{1}{2}}}{3D^{\frac{1}{2}}}\right) = O(1). \tag{4.73}$$

Thus, taking $m = O\left(\log\left(\frac{\overline{\kappa}}{H}\right)\right)$ completes the proof of (4.63). The proof of (4.64) follows from a duality argument as in Lemma 4.1. ∎

We are now ready to establish our main theorem, which estimates the error between the solution p and the multiscale solution p_{ms}.

THEOREM 4.1. *Suppose $f \in [L^2(\Omega)]^2$. Let $m \geq 2$ be the number of coarse grid layers in the oversampling regions in (3.10). Let p be the solution of (2.4) and p_{ms} be the solution of (3.13). If $m = O\left(\log\left(\frac{\overline{\kappa}}{H}\right)\right)$, then we have*

$$\|p(T,\cdot) - p_{ms}(T,\cdot)\|_c^2 + \int_0^T \|p - p_{ms}\|_{a_Q}^2 dt \leq CH^2\underline{\kappa}^{-1}\Lambda^{-1}\left(\|p^0\|_{a_Q}^2 + \int_0^T \|f\|_{[L^2(\Omega)]^2}^2 dt\right). \tag{4.74}$$

Proof. Taking $v = \frac{\partial p}{\partial t}$ in (2.4), we have

$$\left\|\frac{\partial p}{\partial t}\right\|_c^2 + \frac{1}{2}\frac{d}{dt}\|p\|_{a_Q}^2 = \left(f, \frac{\partial p}{\partial t}\right) \leq C\|f\|_{[L^2(\Omega)]^2}^2 + \frac{1}{2}\left\|\frac{\partial p}{\partial t}\right\|_c^2. \tag{4.75}$$

Integrating over $(0,T)$, we have

$$\frac{1}{2}\int_0^T \left\|\frac{\partial p}{\partial t}\right\|_c^2 dt + \frac{1}{2}\|p(T,\cdot)\|_{a_Q}^2 \leq C\left(\|p^0\|_{a_Q}^2 + \int_0^T \|f\|_{[L^2(\Omega)]^2}^2 dt\right). \tag{4.76}$$

Similarly, taking $v = \dfrac{\partial p_{ms}}{\partial t}$ in (3.13) and integrating over $(0,T)$, we have

$$\frac{1}{2}\int_0^T \left\|\frac{\partial p_{ms}}{\partial t}\right\|_c^2 dt + \frac{1}{2}\|p_{ms}(T,\cdot)\|_{a_Q}^2 \leq C\left(\|p^0\|_{a_Q}^2 + \int_0^T \|f\|_{[L^2(\Omega)]^2}^2 dt\right). \tag{4.77}$$

On the other hand, from (2.4), we see that

$$\mathcal{A}p = f - \mathcal{C}\frac{\partial p}{\partial t}, \tag{4.78}$$

and therefore

$$\|\mathcal{A}p\|_{[L^2(\Omega)]^2} \leq C\left(\|f\|_{[L^2(\Omega)]^2} + \left\|\frac{\partial p}{\partial t}\right\|_c\right). \tag{4.79}$$

By the definition of p in (2.4) and p_{ms} in (3.13), for all $v \in V_{ms}, t \in (0,T)$, we have

$$c\left(\frac{\partial (p-p_{ms})}{\partial t}, v\right) + a_Q(p-p_{ms}, v) = 0. \tag{4.80}$$

Therefore, we have

$$\begin{aligned}
&\frac{1}{2}\frac{d}{dt}\|p-p_{ms}\|_c^2 + \|p-p_{ms}\|_{a_Q}^2 \\
&= c\left(\frac{\partial (p-p_{ms})}{\partial t}, p-p_{ms}\right) + a_Q(p-p_{ms}, p-p_{ms}) \\
&= c\left(\frac{\partial (p-p_{ms})}{\partial t}, p-R_{ms}p\right) + a_Q(p-p_{ms}, p-R_{ms}p) \\
&\leq \left\|\frac{\partial (p-p_{ms})}{\partial t}\right\|_c \|p-R_{ms}p\|_c + \|p-p_{ms}\|_{a_Q}\|p-R_{ms}p\|_{a_Q} \\
&\leq \left(\left\|\frac{\partial p}{\partial t}\right\|_c + \left\|\frac{\partial p_{ms}}{\partial t}\right\|_c\right)\|p-R_{ms}p\|_c + \frac{1}{2}\|p-p_{ms}\|_{a_Q}^2 + \frac{1}{2}\|p-R_{ms}p\|_{a_Q}^2.
\end{aligned} \tag{4.81}$$

Integrating over $(0,T)$ and using (4.79) with Lemma 4.4, we have

$$\begin{aligned}
&\frac{1}{2}\|p(T,\cdot)-p_{ms}(T,\cdot)\|_c^2 + \frac{1}{2}\int_0^T \|p-p_{ms}\|_{a_Q}^2 dt \\
&\leq \int_0^T \left(\left\|\frac{\partial p}{\partial t}\right\|_c + \left\|\frac{\partial p_{ms}}{\partial t}\right\|_c\right)\|p-R_{ms}p\|_c dt + \frac{1}{2}\int_0^T \|p-R_{ms}p\|_{a_Q}^2 dt \\
&\leq \left(\int_0^T \left(\left\|\frac{\partial p}{\partial t}\right\|_c + \left\|\frac{\partial p_{ms}}{\partial t}\right\|_c\right)^2 dt\right)^{\frac{1}{2}} \left(\int_0^T \|p-R_{ms}p\|_c^2 dt\right)^{\frac{1}{2}} + \frac{1}{2}\int_0^T \|p-R_{ms}p\|_{a_Q}^2 dt \\
&\leq \left(\int_0^T \left(\left\|\frac{\partial p}{\partial t}\right\|_c + \left\|\frac{\partial p_{ms}}{\partial t}\right\|_c\right)^2 dt\right)^{\frac{1}{2}} \left(\int_0^T C H^4 \underline{\kappa}^{-2}\Lambda^{-2}\left(\|f\|_{[L^2(\Omega)]^2} + \left\|\frac{\partial p}{\partial t}\right\|_c\right)^2 dt\right)^{\frac{1}{2}}
\end{aligned}$$

$$+\int_0^T CH^2\underline{\kappa}^{-1}\Lambda^{-1}\left(\|f\|_{[L^2(\Omega)]^2}+\left\|\frac{\partial p}{\partial t}\right\|_c\right)^2 dt$$
$$\leq CH^2\underline{\kappa}^{-1}\Lambda^{-1}\int_0^T\left(\left\|\frac{\partial p}{\partial t}\right\|_c^2+\left\|\frac{\partial p_{ms}}{\partial t}\right\|_c^2+\|f\|^2_{[L^2(\Omega)]^2}\right)dt. \tag{4.82}$$

Finally, combining (4.76), (4.77) and (4.82), we obtain our desired result. ∎

5. Numerical examples

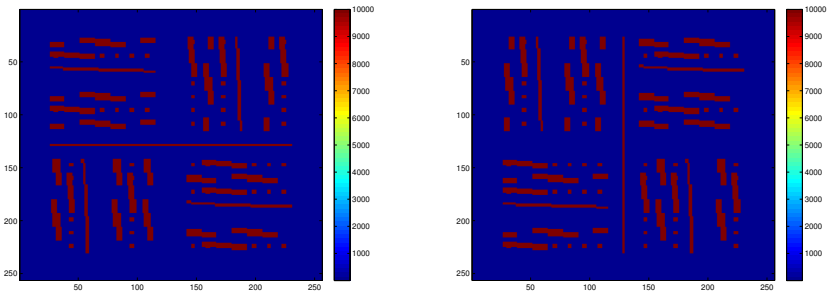

FIG. 5.1. *Media used in numerical experiments. κ_1 (left) and κ_2 (right).*

In this section, we present two numerical examples. We perform numerical experiments with high-contrast media to see the orders of convergence of our proposed method in energy norm and L^2 norm. We will also study the effects of the number of oversampling layers m on the quality of the approximations. In all the experiments, we take the spatial domain to be $\Omega=(0,1)^2$ and the fine mesh size to be $h=1/256$. An example of the media κ_1 and κ_2 used in the experiments is illustrated in Figure 5.1. In the figure, the contrast values, i.e. the ratio of the maximum and the minimum in Ω, of the media are $\overline{\kappa}_1=10^4$ and $\overline{\kappa}_2=10^4$. We will also see the effects of the contrast values of the media on the error, while the configurations of the media remain unchanged.

5.1. Experiment 1. In this experiment, we consider the dual continuum model in the steady state, i.e.

$$\begin{aligned}-\text{div}(\kappa_1\nabla p_1)+\sigma(p_1-p_2)&=f_1,\\ -\text{div}(\kappa_2\nabla p_2)-\sigma(p_1-p_2)&=f_2,\end{aligned} \tag{5.1}$$

where the configuration of the media κ_1 and κ_2 are illustrated in Figure 5.1. The conductivity values in the background are fixed to be $\kappa_1^m=1$ and $\kappa_2^m=1$, while the conductivity values κ_1^f and κ_2^f in the channels are high. The physical parameter for mass transfer is set to be $\sigma=1$. The source functions are taken as $f_1(x,y)=2\pi^2\sin(\pi x)\sin(\pi y)$ and $f_2(x,y)=1$ for all $(x,y)\in\Omega$. The steady-state Equation (5.1) has a weak formulation: find $p=(p_1,p_2)$ with $p_i\in V$ such that

$$a_Q(p,v)=(f,v), \tag{5.2}$$

for all $v=(v_1,v_2)$ with $v_i\in V$. The numerical solution is then given by: find $p_{ms}=(p_{ms,1},p_{ms,2})$ with $p_{ms,i}\in V_{ms}$ such that

$$a_Q(p_{ms},v)=(f,v), \tag{5.3}$$

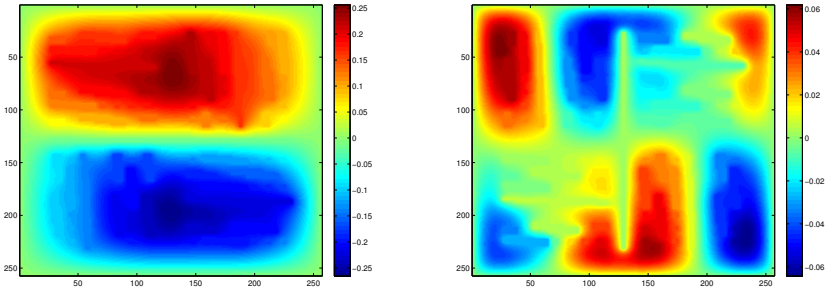

FIG. 5.2. *Plots of numerical solution: $p_{ms,1}$ (left) and $p_{ms,2}$ (right)*

H	m	a_Q error	order	L^2 error	order
1/8	4	33.4293%	–	15.8783%	–
1/16	6	5.7191%	2.55	0.6265%	4.66
1/32	7	1.2437%	2.20	0.0504%	3.64
1/64	9	0.3585%	1.79	0.0067%	2.91

TABLE 5.1. *History of convergence with* 6 *basis functions in Experiment 1.*

H	m	a_Q error	order	L^2 error	order
1/8	4	43.9247%	–	34.2923%	–
1/16	6	7.7963%	2.49	1.0463%	5.03
1/32	7	1.5417%	2.34	0.0709%	3.88
1/64	9	0.4993%	1.63	0.0124%	2.52

TABLE 5.2. *History of convergence with* 4 *basis functions in Experiment 1.*

m	$\overline{\kappa}=10^4$	$\overline{\kappa}=10^5$	$\overline{\kappa}=10^6$
3	22.4683%	51.0835%	69.4279%
4	6.3274%	10.1892%	25.6786%
5	5.7205%	5.7978%	6.4329%
6	5.7122%	5.7220%	5.7231%

TABLE 5.3. *Comparison of a_Q error with different number of layers m and contrast value $\overline{\kappa}$ in Experiment 1.*

for all $v=(v_1,v_2)$ with $v_i\in V_{ms}$. In other words, we have $p_{ms}=R_{ms}p$ according to the definition (4.7), and the theoretical orders of convergence follow Lemma 4.4.

Figure 5.2 illustrates the numerical solution of the steady-state flow problem. Tables 5.1–5.3 record the error in L^2 norm and a_Q norm with various settings. In Table 5.1, we take the conductivity values in the channels to be $\kappa_1^f=10^4$ and $\kappa_2^f=10^6$. We use 6 basis functions per oversampled region since there are 6 small eigenvalues in the spectrum, and according to our analysis, we need to include the first 6 spectral basis functions in the auxiliary space to have good convergence. As we refine coarse mesh size H, we fix the number of oversampling layers to be $m\approx 9\log(1/H)/\log(64)$, which is suggested by our analysis. The results show that the numerical approximations are very accurate, and the errors converge with refinement of the coarse mesh size. Table 5.2 shows the same quantities when the number of basis functions used in each coarse region is reduced to 4. By comparing to Table 5.1, it can be seen that the errors are larger than those when we use 6 basis functions. Figure 5.3 depicts the log-log plot (in exponential base)

of L^2 error and energy error against coarse mesh size H. The least-squares fit suggests that we obtain a better convergence order in our numerical experiment compared with the theoretical result. Table 5.3 compares the a_Q error with various combinations of number of layers m and contrast value $\overline{\kappa}$, where the conductivity values in the channels are the same, with 6 basis functions per coarse region and coarse mesh size $H = 1/16$. It can be seen that with a larger oversampled region, the error decreases. On the other hand, the error increases with the contrast value.

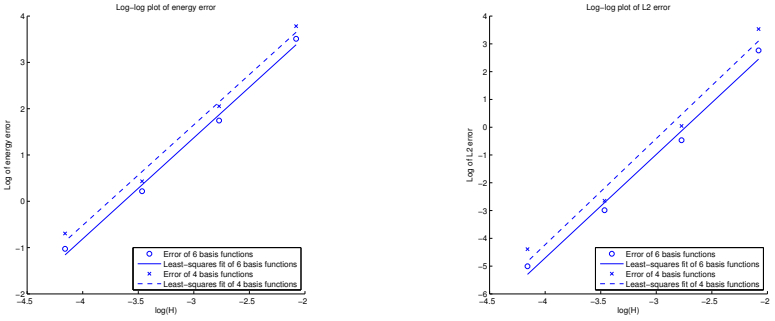

FIG. 5.3. *Log-Log plot for errors in Experiment 1. Left: energy error; the slope for 6 basis functions is 2.18 and for 4 basis functions is 2.17. Right: L^2 error; the slope for 6 basis functions is 3.73 and for 4 basis functions is 3.82.*

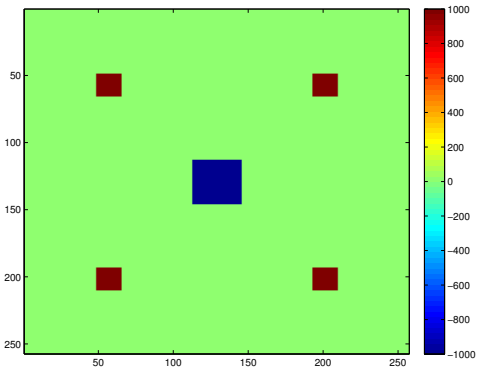

FIG. 5.4. *Source function f_2 in Experiment 2.*

H	m	Δt	a_Q error	order	L^2 error	order
1/8	4	1	92.0441%	–	58.6453%	–
1/16	6	0.5	20.9725%	2.13	5.2984%	3.47
1/32	7	0.25	6.7504%	1.64	0.7718%	2.78
1/64	9	0.125	1.9074%	1.82	0.0934%	3.05

TABLE 5.4. *History of convergence with 6 basis functions in Experiment 2.*

5.2. Experiment 2. In this experiment, we consider the time-dependent dual continuum model (2.1). We are interested in finding a numerical approximation in

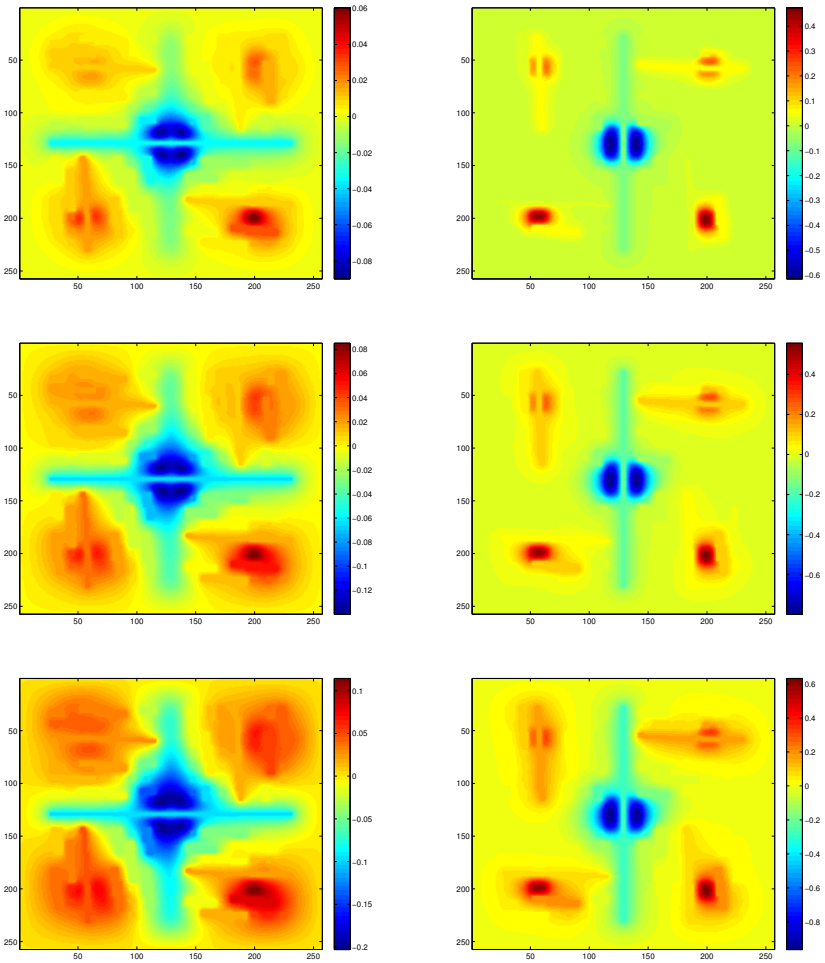

FIG. 5.5. *Plots of numerical solution at different time instants: $p_{ms,1}$ (left) and $p_{ms,2}$ (right) in Experiment 2.*

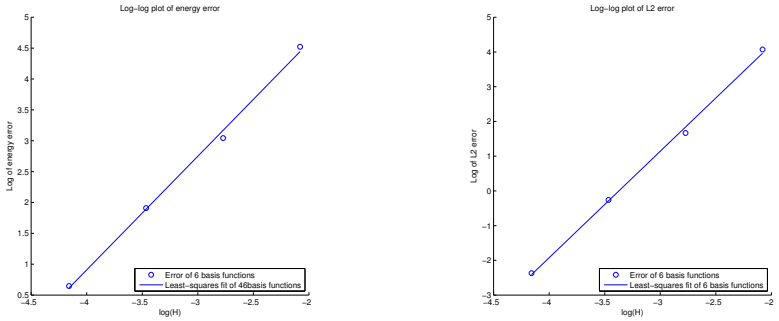

FIG. 5.6. *Log-Log plot for errors in Experiment 2. Left: energy error; the slope for 6 basis functions is 1.84. Right: L^2 error; the slope for 6 basis functions is 3.07.*

the temporal domain $[0,T]$, where the final time is set to be $T=5$. The configuration of the media κ_1 and κ_2 are illustrated in Figure 5.1. The conductivity values in the background are set to be $\kappa_1^m=10^{-1}$ and $\kappa_2^m=10^0$, while the values in the channels are taken as $\kappa_1^f=10^4$ and $\kappa_2^f=10^6$. The velocities in the background are taken as $c_1^m=10^1$ and $c_2^m=10^3$, while the values in the channels are taken as $c_1^f=10^2$ and $c_2^f=10^4$. The physical parameter for mass transfer is set to be $\sigma=25$. The source functions are taken as time-independent, where $f_1(t,x,y)=0$ for all $(t,x,y)\in[0,T]\times\Omega$ and f_2 is depicted in Figure 5.4. The initial condition is given as $p_1(0,x,y)=0$ and $p_2(0,x,y)=0$ for all $(x,y)\in\Omega$.

Figure 5.5 illustrates the numerical solutions at time instants $t=1.25$, $t=2.5$ and $t=5$ respectively. Table 5.4 records the error in L^2 norm and a_Q norm with 6 basis functions per oversampled region and number of oversampling layers set to be $m\approx 9\log(1/H)/\log(64)$. Again, the results show that the numerical approximations are very accurate, and the errors converge with refinement of the coarse mesh size. Figure 5.6 shows the log-log plots of the energy error and L^2 error against coarse mesh size H in exponential base. The least-squares fits again illutstrate our method provides good convergence rates.

6. Conclusions

In this paper, we present the CEM-GMsFEM for a dual continuum model. The method is based on a set of multiscale basis functions. To find the basis, we first obtain the auxiliary basis functions, which are important to identify high contrast channels and fracture networks. Then, we solve an energy minimization problem with some constraints related to the auxiliary functions. We show that the basis functions are localized and that the resulting method has a mesh-dependent convergence. Finally, we present some numerical results to confirm the theory.

Acknowledgements. EC's work is partially supported by Hong Kong RGC General Research Fund (Project 14304217) and CUHK Direct Grant for Research 2017-18. MV's work is supported by the mega-grant of the Russian Federation Government (N 14.Y26.31.0013). YE would like to thank the partial support from NSF 1620318 and 1934904. YE would also like to acknowledge the support of Mega-grant of the Russian Federation Government (N 14.Y26.31.0013).

REFERENCES

[1] I.Y. Akkutlu, Y. Efendiev, and M. Vasilyeva, *Multiscale model reduction for shale gas transport in fractured media*, Comput. Geosci., 20(5):953–973, 2016. 1

[2] I.Y. Akkutlu and E. Fathi, *Multiscale gas transport in shales with local kerogen heterogeneities*, Soc. Pet. Eng. J., 17(04):1–002, 2012. 1

[3] T. Arbogast, J. Douglas Jr., and U. Hornung, *Derivation of the double porosity model of single phase flow via homogenization theory*, SIAM J. Math. Anal., 21(4):823–836, 1990. 1

[4] R.G. Baca, R.C. Arnett, and D.W. Langford, *Modelling fluid flow in fractured-porous rock masses by finite-element techniques*, Int. J. Numer. Meth. Fluids, 4(4):337–348, 1984. 1

[5] G.I. Barenblatt, I.P. Zheltov, and I.N. Kochina, *Basic concepts in the theory of seepage of homogeneous liquids in fissured rocks [strata]*, J. Appl. Math. Mech., 24(5):1286–1303, 1960. 1, 2

[6] I.I. Bogdanov, V.V. Mourzenko, J.-F. Thovert, and P.M. Adler, *Two-phase flow through fractured porous media*, Phys. Rev. E, 68(2):026703, 2003. 1

[7] E.T. Chung, Y. Efendiev, and T.Y. Hou, *Adaptive multiscale model reduction with generalized multiscale finite element methods*, J. Comput. Phys., 320:69–95, 2016. 1

[8] E.T. Chung, Y. Efendiev, and W.T. Leung, *Constraint energy minimizing generalized multiscale finite element method in the mixed formulation*, Comput. Geosci., 22(3):677–693, 2018. 1

[9] E.T. Chung, Y. Efendiev, R.L Gibson Jr., and M. Vasilyeva, *A generalized multiscale finite element method for elastic wave propagation in fractured media*, Int. J. Geomath., 7:163–182, 2016. 1

[10] E.T. Chung, Y. Efendiev, W.T. Leung, and M. Vasilyeva, *Coupling of multiscale and multi-continuum approaches*, Int. J. Geomath., 8(1):9–41, 2017. 1

[11] E.T. Chung, Y. Efendiev, and W.T. Leung, *Residual-driven online generalized multiscale finite element methods*, J. Comput. Phys., 302:176–190, 2015. 1

[12] E.T. Chung, Y. Efendiev, and W.T. Leung, *Constraint energy minimizing generalized multiscale finite element method*, Comput. Meth. Appl. Mech. Eng., 339:298–319, 2018. 1

[13] E.T. Chung, Y. Efendiev, and W.T. Leung, *Fast online generalized multiscale finite element method using constraint energy minimization*, J. Comput. Phys., 355:450–463, 2018. 1

[14] E.T. Chung, Y. Efendiev, and G. Li, *An adaptive GMsFEM for high-contrast flow problems*, J. Comput. Phys., 273:54–76, 2014. 1

[15] J. Douglas Jr. and T. Arbogast, *Dual porosity models for flow in naturally fractured reservoirs*, in J. Cushman (Ed.), Dynamics of Fluids in Hierarchical Porous Media, Academic Press, 177–221, 1990. 1, 2

[16] L.J. Durlofsky, *Numerical calculation of equivalent grid block permeability tensors for heterogeneous porous media*, Water Resour. Res., 27:699–708, 1991. 1

[17] Y. Efendiev, J. Galvis, and T. Hou, *Generalized multiscale finite element methods*, J. Comput. Phys., 251:116–135, 2013. 1

[18] B. Eikemo, K.-A. Lie, G.T. Eigestad, and H.K. Dahle, *Discontinuous Galerkin methods for advective transport in single-continuum models of fractured media*, Adv. Water Resour., 32(4):493–506, 2009. 1

[19] J. Erhel, J.-R. De Dreuzy, and B. Poirriez, *Flow simulation in three-dimensional discrete fracture networks*, SIAM J. Sci. Comput., 31(4):2688–2705, 2009. 1

[20] J. Galvis and Y. Efendiev, *Domain decomposition preconditioners for multiscale flows in high contrast media. Reduced dimensional coarse spaces*, SIAM J. Multiscale Model. Simul., 8:1621–1644, 2010. 1

[21] S. Geiger-Boschung, S.K. Matthäi, J. Niessner, and R. Helmig, *Black-oil simulations for three-component, three-phase flow in fractured porous media*, Soc. Pet. Eng. J., 14(02):338–354, 2009. 1

[22] S. Granet, P. Fabrie, P. Lemonnier, and M. Quintard, *A two-phase flow simulation of a fractured reservoir using a new fissure element method*, J. Pet. Sci. Eng., 32(1):35–52, 2001. 1

[23] H. Hoteit and A. Firoozabadi, *Multicomponent fluid flow by discontinuous Galerkin and mixed methods in unfractured and fractured media*, Water Resour. Res., 41(11):W1142, 2005. 1

[24] H. Hoteit and A. Firoozabadi, *An efficient numerical model for incompressible two-phase flow in fractured media*, Adv. Water Resour., 31(6):891–905, 2008. 1

[25] T.Y. Hou and P. Zhang, *Sparse operator compression of higher-order elliptic operators with rough coefficients*, Res. Math. Sci., 4(1):24, 2017. 1

[26] R. Juanes, J. Samper, and J. Molinero, *A general and efficient formulation of fractures and boundary conditions in the finite element method*, Int. J. Numer. Meth. Eng., 54(12):1751–1774, 2002. 1

[27] M. Karimi-Fard and L.J. Durlofsky, *A general gridding, discretization, and coarsening methodology for modeling flow in porous formations with discrete geological features*, Adv. Water Resour., 96:354–372, 2016. 1

[28] M. Karimi-Fard, L.J. Durlofsky and K. Aziz, *An efficient discrete-fracture model applicable for general-purpose reservoir simulators*, Soc. Pet. Eng. J., 9(02):227–236, 2004. 1

[29] M. Karimi-Fard and A. Firoozabadi, *Numerical simulation of water injection in fractured media using the discrete-fracture model and the Galerkin method*, Soc. Pet. Eng. Reserv. Eval. Eng., 6(02):117–126, 2003. 1

[30] H. Kazemi, L.S. Merrill Jr., K.L. Porterfield and P.R. Zeman, *Numerical simulation of water-oil flow in naturally fractured reservoirs*, Soc. Pet. Eng. J., 16(06):317–326, 1976. 1

[31] H.H. Kim, E. Chung, and J. Wang, *BDDC and FETI-DP algorithms with adaptive coarse spaces for three-dimensional elliptic problems with oscillatory and high contrast coefficients*, J. Comput. Phys., 349:191–214, 2017. 1

[32] H.H. Kim and E.T. Chung, *A BDDC algorithm with enriched coarse spaces for two-dimensional elliptic problems with oscillatory and high contrast coefficients*, Multiscale Model. Simul., 13(2):571–593, 2015. 1

[33] J.-G. Kim and M.D. Deo, *Finite element, discrete-fracture model for multiphase flow in porous media*, AIChE J., 46(6):1120–1130, 2000. 1

[34] J. Ma, G.D. Couples, and S.D. Harris, *A mixed finite element technique based on implicit discretization of faults for permeability upscaling in fault damage zones*, Water Resour. Res.,

42(8):W08413, 2006. 1

[35] A. Målqvist and D. Peterseim, *Localization of elliptic multiscale problems*, Math. Comput., 83(290):2583–2603, 2014. 1

[36] V. Martin, J. Jaffré, and J.E. Roberts, *Modeling fractures and barriers as interfaces for flow in porous media*, SIAM J. Sci. Comput., 26(5):1667–1691, 2005. 1

[37] S.K. Matthai, A.A. Mezentsev, and M. Belayneh, *Finite element-node-centered finite-volume two-phase-flow experiments with fractured rock represented by unstructured hybrid-element meshes*, Soc. Pet. Eng. Reserv. Eval. Eng., 10(06):740–756, 2007. 1

[38] J.E.P. Monteagudo and A. Firoozabadi, *Control-volume method for numerical simulation of two-phase immiscible flow in two- and three-dimensional discrete-fractured media*, Water Resour. Res., 40(7):W07405, 2004. 1

[39] H.M. Nick and S.K. Matthäi, *Comparison of three FE-FV numerical schemes for single-and two-phase flow simulation of fractured porous media*, Transp. Porous Media, 90(2):421–444, 2011. 1

[40] B. Noetinger, *A quasi steady state method for solving transient Darcy flow in complex 3D fractured networks accounting for matrix to fracture flow*, J. Comput. Phys., 283:205–223, 2015. 1

[41] H. Owhadi, *Multigrid with rough coefficients and multiresolution operator decomposition from hierarchical information games*, SIAM Rev., 59(1):99–149, 2017. 1

[42] H. Owhadi, L. Zhang, and L. Berlyand, *Polyharmonic homogenization, rough polyharmonic splines and sparse super-localization*, ESAIM Math. Model. Numer. Anal., 48(2):517–552, 2014. 1

[43] K. Pruess and T.N. Narasimhan, *On fluid reserves and the production of superheated steam from fractured, vapor-dominated geothermal reservoirs*, J. Geophys. Res. Solid Earth, 87(B11):9329–9339, 1982. 1

[44] V. Reichenberger, H. Jakobs, P. Bastian, and R. Helmig, *A mixed-dimensional finite volume method for two-phase flow in fractured porous media*, Adv. Water Resour., 29(7):1020–1036, 2006. 1

[45] M. Wang, S.W. Cheung, E.T. Chung, M. Vasilyeva, and Y. Wang, *Generalized multiscale multicontinuum model for fractured vuggy carbonate reservoirs*, J. Comput. Appl. Math., 366:112370, 2020. 1

[46] J.E. Warren, and P.J. Root, *The behavior of naturally fractured reservoirs*, Soc. Pet. Eng. J., 3(03):245–255, 1963. 1, 2

[47] X.H. Wu, Y. Efendiev, and T.Y. Hou, *Analysis of upscaling absolute permeability*, Discrete Contin. Dyn. Syst. Ser. B., 2:158–204, 2002. 1

[48] Y.-S. Wu, Y. Di, Z. Kang, and P. Fakcharoenphol, *A multiple-continuum model for simulating single-phase and multiphase flow in naturally fractured vuggy reservoirs*, J. Petrol. Sci. Eng., 78(1):13–22, 2011. 1

[49] Y.-S. Wu, and K. Pruess, *A multiple-porosity method for simulation of naturally fractured petroleum reservoirs*, Soc. Pet. Eng. Reserv. Eng., 3(01):327–336, 1988. 1

[50] Y.-S. Wu, G. Qin, R.E. Ewing, Y. Efendiev, Z. Kang, and Y. Ren, *A multiple-continuum approach for modeling multiphase flow in naturally fractured vuggy petroleum reservoirs*, in International Oil & Gas Conference and Exhibition in China, Soc. Pet. Eng., 2006. 1